Optimization of growth of large-area SnS thin films and heterostructures for spin pumping and spin-orbit torque

Himanshu Bangar, Pankhuri Gupta, Rajendra Singh, and Pranaba Kishor Muduli*
Department of Physics, Indian Institute of Technology Delhi, Hauz Khas, New Delhi 110016, India

Sheetal Dewan
School of Interdisciplinary Research, Indian Institute of Technology Delhi, Hauz Khas, New Delhi 110016, India

Samaresh Das
Center for Applied Research in Electronics, Indian Institute of Technology Delhi, Hauz Khas, New Delhi 110016, India

(Received 24 April 2023; revised 30 July 2023; accepted 28 August 2023; published 25 September 2023)

Two-dimensional (2D) van der Waals materials are promising for spintronics due to their unique physical properties down to the monolayer thickness. Tin monosulfide (SnS) is a van der Waals material belonging to the monochalcogenide family, lacking mirror symmetry in its crystal structure. Monolayer SnS also exhibits spin-splitting band structure as well as in-plane ferroelectricity. In this work, we investigate the potential of SnS for spintronic applications by optimizing the growth of large-area 2D thin films of SnS on a CMOS-compatible Si/SiO_2 substrate using pulsed laser deposition. We perform a comprehensive SnS thickness-dependent spin pumping study in $SnS/Ni_{80}Fe_{20}$ system for SnS films grown at 300 and 473 K. The thickness dependence of the damping constant of $Ni_{80}Fe_{20}$ agreed with the theory of spin pumping only for optimized SnS layers grown at 300 K, exhibiting low and thickness-independent surface roughness. The effective spin mixing conductance of $SnS/Ni_{80}Fe_{20}$ for optimized SnS layers grown at 300 K is estimated to be $(8.83 \pm 1.15)\ \mathrm{nm}^{-2}$. We also performed spin-torque ferromagnetic resonance (STFMR) measurements on the SnS (1.3 nm)/$Ni_{80}Fe_{20}$ devices for the optimized SnS layers grown at 300 K. Through angle-resolved STFMR measurements, we show the presence of unconventional spin-orbit torques in SnS. Our findings suggest that SnS is promising for emerging spintronic devices.

DOI: 10.1103/PhysRevMaterials.7.094406

I. INTRODUCTION

Spintronic devices offer high speed, endurance, and reduced power consumption, which are crucial for the next-generation electronic devices [1]. One of the essential requirements for practical applications is the efficient generation of pure spin current. The electrical currents can be converted to spin currents in heterostructures consisting of ferromagnet and nonmagnetic materials by using phenomena such as the direct spin Hall effect (SHE) [2,3] and the Rashba-Edelstein effect (REE) [4,5]. The spin current can exert a spin-orbit torque (SOT) on the magnetization of the ferromagnet, enabling magnetization switching and domain wall motion [6] for low-power memory and logic applications [7]. Such SOT-based devices often consist of ferromagnet (FM)/heavy metal (HM) heterostructures. Recently, two-dimensional (2D) materials and interfaces have attracted a lot of interest for SOT-based devices [8,9]. 2D materials with low crystalline symmetry-based systems can generate out-of-plane damping like torque [10] essential for efficient switching of perpendicularly magnetized systems used in high-density magnetic recording [11]. MacNeill *et al.* reported an out-of-plane dampinglike torque in a low symmetry transition metal dichalcogenide (TMD) WTe_2/Permalloy bilayers [10]. Subsequently, several TMD based heterostructures were investigated for SOT applications [4,10,12–15]. Furthermore, TMDs offer large and controllable spin-charge conversion via REE in TMD/FM bilayers [4,5]. However, 2D monochalcogenides are yet to be explored for spintronic applications.

In recent years, group-IV monochalcogenides (MX; M = Sn/Ge and X = S/Se) have drawn a lot of attention due to their intriguing properties, such as excellent carrier mobility [16], thermoelectricity [17], piezoelectricity [18], and strong in-plane ferroelectricity [19–21]. Tin monosulfide (SnS) is a van der Waals material belonging to the monochalcogenide family that also exhibits purely in-plane ferroelectricity in monolayer form [22]. Furthermore, the ferroelectricity of SnS can be tuned by the gate voltage [21]. These characteristics are highly promising for a wide variety of applications of SnS such as sensors [23] and memories [24].

SnS exhibits an orthorhombic lattice structure with space group *Pnma* similar to black phosphorous [25]. Figure 1(a) shows the side view of the SnS bilayer along the *b* axis. The SnS structure lacks mirror symmetry about the plane shown by the vertical dashed line, which makes it promising for SOT applications [26]. SnS also exhibits finite and strain tunable spin splitting [27]. In addition, the ferroelectric nature of SnS

*muduli@physics.iitd.ac.in

 ©2023 American Physical Society

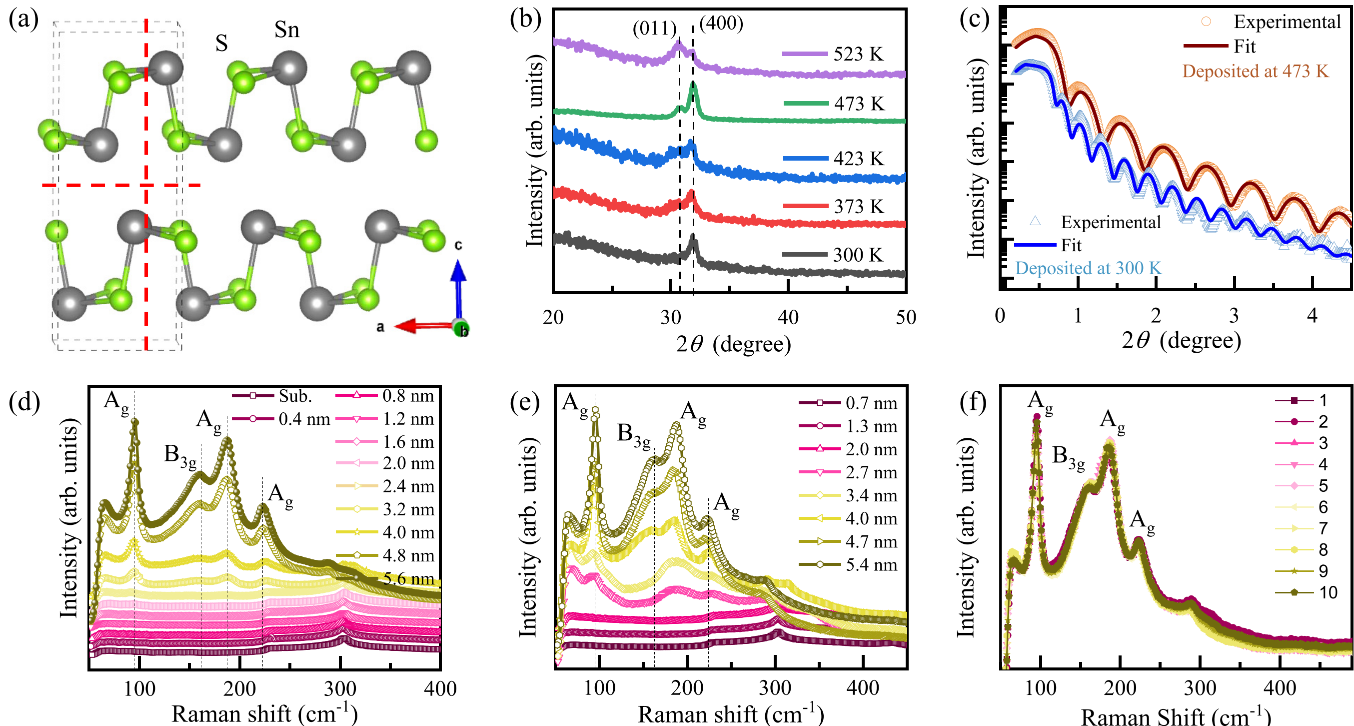

FIG. 1. (a) A schematic side view of the structure of bilayer SnS. (b) X-ray diffraction (XRD) data for SnS thin film grown at various substrate temperatures (T_S). (c) X-ray reflectivity (XRR) data and corresponding fits (solid line) for samples deposited at 473 K (open circle) and room temperature, 300 K (open triangle). Acquired Raman spectra for samples grown at (d) 473 K and (e) 300 K with different thicknesses. (f) Raman spectra at ten different spots on the same large area SnS thin film of thickness 5.4 nm.

can allow electric field control of spin-charge conversion, leading to reduced power consumption. Despite these intriguing properties, SnS has not been explored for spintronics applications, and the studies are limited to ferroelectric [22] and optoelectronic applications [28].

The first step in realizing the application potential of SnS is the 2D growth of high-quality SnS thin films on CMOS-compatible substrates. However, the growth of SnS thin films is quite challenging due to the existence of several Sn-S phases, such as SnS, SnS_2, Sn_2S_3, Sn_3S_4, and Sn_4S_5 [29]. SnS thin films have been grown using a variety of techniques, including liquid exfoliation [30], physical vapor deposition [31], and molecular beam epitaxy [21]. Some of these techniques require toxic H_2S gas to control the chemical composition of SnS thin films. Pulsed laser deposition (PLD) is an appealing alternative since it permits H_2S-free growth and results in the formation of a single SnS phase [29]. However, the PLD growth of SnS has been demonstrated only for thick SnS films (∼150 nm) on MgO [32] and glass substrates [29]. The reports on the growth of a few layers of SnS on Si/SiO_2 using PLD are very much limited to the work by Wang *et al.* [28]. In their work, Wang *et al.* grew SnS films at 473 K and then post-annealed the films at 573 K for 1 hr. High-temperature growth and post-annealing might result in off-stoichiometric composition due to the desorption of S. Hence, low-temperature deposition without annealing is highly desirable for the growth of high-quality SnS thin films.

In this article, we demonstrate the high-quality 2D growth of few-layer SnS on CMOS-compatible Si/SiO_2 substrates using the PLD technique. We demonstrate that ultrathin SnS films can be grown at room temperature by optimizing the growth conditions. We perform a comprehensive thickness-dependent spin pumping study in the $SnS/Ni_{80}Fe_{20}$ (hereafter $Ni_{80}Fe_{20}$ = Py) system for SnS layers grown at 300 K and 473 K. We demonstrate that the deposition of SnS at 300 K helps in reducing the roughness of the films and also improves the quality of the Py layer. For the optimized stack (SnS grown at 300 K), we estimate the effective spin mixing conductance to be (8.83 ± 1.15) nm^{-2}. Finally, we performed spin-torque ferromagnetic resonance (STFMR) experiments on SnS (1.3 nm)/Py (8 nm)-based devices. From detailed angular-dependent STFMR measurements, we found unconventional SOTs in SnS (1.3 nm)/Py (8 nm). The results show that few-layer ferroelectric SnS is a promising material for developing efficient spintronic devices.

II. EXPERIMENTAL METHODS

SnS thin films were grown on Si/SiO_2 substrate by PLD technique using a commercially procured SnS target. A pulsed KrF excimer laser (operated at 248 nm) was used for ablating the target at a repetition rate of 5 Hz, maintaining a laser fluence of 1.1 J cm^{-2}. The working pressure during the deposition was 1 $\times 10^{-4}$ mBar in a pure Ar gas atmosphere. The target to substrate distance was 5 cm. The growth temperature was varied from 300 K to 523 K. The SnS film thickness was precisely controlled by the number of laser shots. After the growth of SnS film, the samples were transferred to an ultrahigh vacuum magnetron sputtering (AJA Orion 8) chamber for the deposition of Py(8 nm)/AlO_x(3 nm)

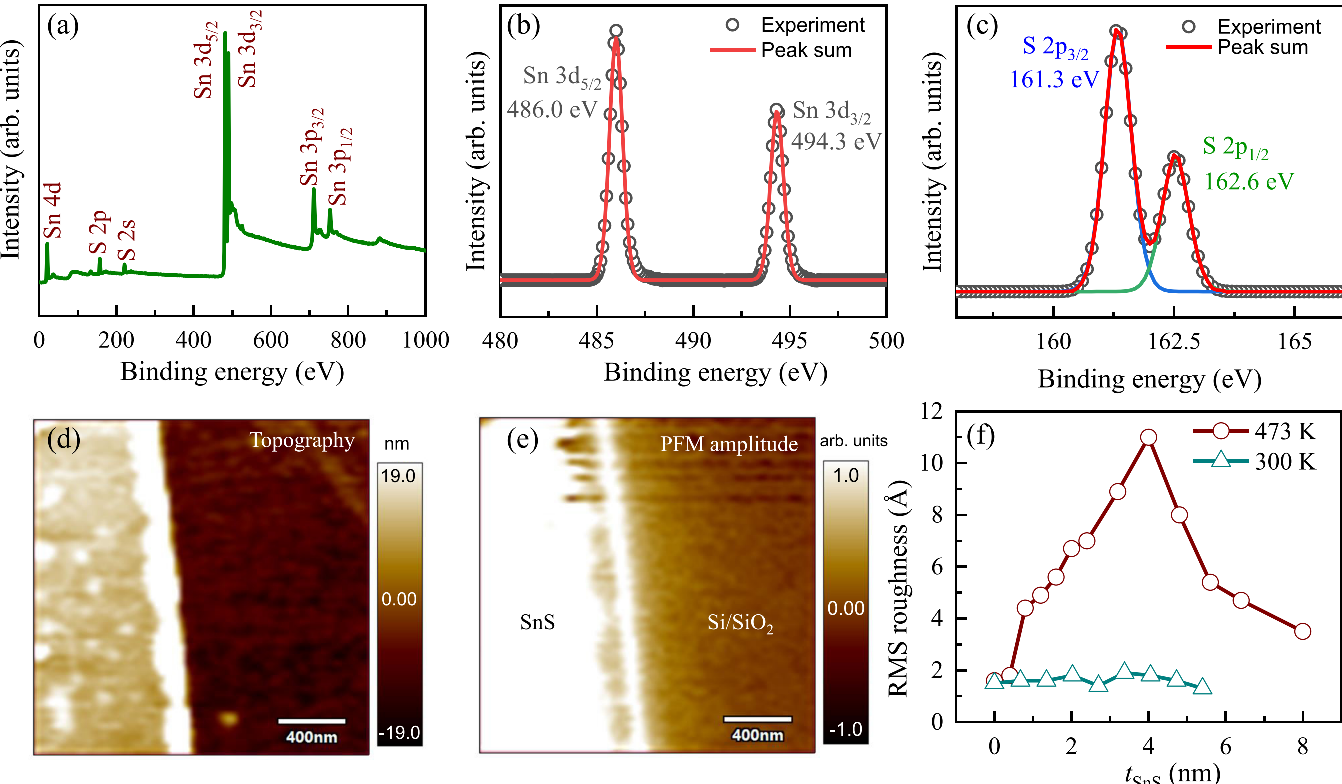

FIG. 2. (a) XPS survey spectrum of SnS sample deposited at 300 K. (b) High-resolution XPS spectrum and its fit showing peaks of Sn 3*d* binding energies at 486.0 and 494.3 eV. (c) High-resolution deconvoluted XPS spectrum and its fit showing peaks of S 2*p* binding energies at 161.3 and 162.6 eV. (d) AFM topography near a SnS step. (e) Lateral PFM response showing the contrast between substrate and SnS. (f) The trend of RMS roughness of SnS thin films deposited at 300 K and 473 K. The roughness is determined from the AFM scans as a function of film thickness (t_{SnS}).

on top of SnS. The Al layer was deposited as a capping layer to avoid oxidation of Py. The growth rate of the Py and Al layer was 0.23 Å/s and 0.20 Å/s, respectively. The base pressure of the sputtering chamber was better than 5×10^{-8} Torr, while the working pressure during deposition was maintained at 2×10^{-3} Torr. We used a lift-off-based fabrication process for the preparation of SnS/Py/Al microstrip devices.

The crystalline quality of the SnS films was characterized using high-resolution x-ray diffraction (HR-XRD) using a PANalytical x-ray diffractometer equipped with a Cu K_α ($\lambda = 1.5406$ Å) source. The Raman data was acquired using a Renishaw inVia confocal microscope with a 532 nm laser wave length and 2400 lines per mm grating at 5 mW power. We performed the scanning electron microscopy (SEM) and energy dispersive x-ray (EDX) measurements using a Jeol SM-7800F prime field emission SEM system. The surface chemistry of the grown SnS films was studied using x-ray photoelectron spectroscopy (XPS) measurements (Kratos Analytical Ltd., AXIS supra system). The surface roughness and morphology were determined by atomic force microscopy (AFM) scans (Asylum Research, MFP-3D system). The AFM images were obtained in the tapping mode using Asylum Research probes (AC240TS-R3) cantilevers. The piezo force microscopy (PFM) scan was performed with Asylum Research probes (ASYELEC-01-R2) conducting cantilever coated with Ti/Ir.

The broadband FMR spectroscopy technique was used to characterize the magnetization dynamics of SnS/Py bilayer thin films as shown schematically in Fig. 3(a). A field modulation technique with lock-in-based detection was employed to enhance the sensitivity of FMR measurements [3,33]. For this purpose, the external DC field was modulated with a low-frequency ac field generated in the Helmholtz coils using the lock-in amplifier. The RF excitation frequency was varied from 3 to 8 GHz. The FMR spectrum obtained by field sweep was then fitted using the derivative of the Lorentzian line-

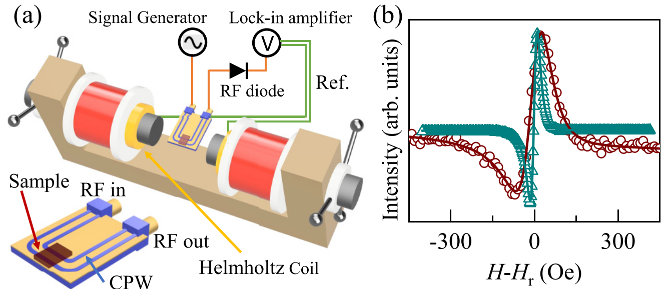

FIG. 3. (a) Schematic illustrating FMR measurement setup in which an RF current is applied to coplanar wave guide (CPW), generating an RF field which drives Py magnetization into resonance. (b) Comparative FMR spectrum measured at 4 GHz for Py/SnS bilayer with SnS layer grown at 473 K (brown) and 300 K (cyan).

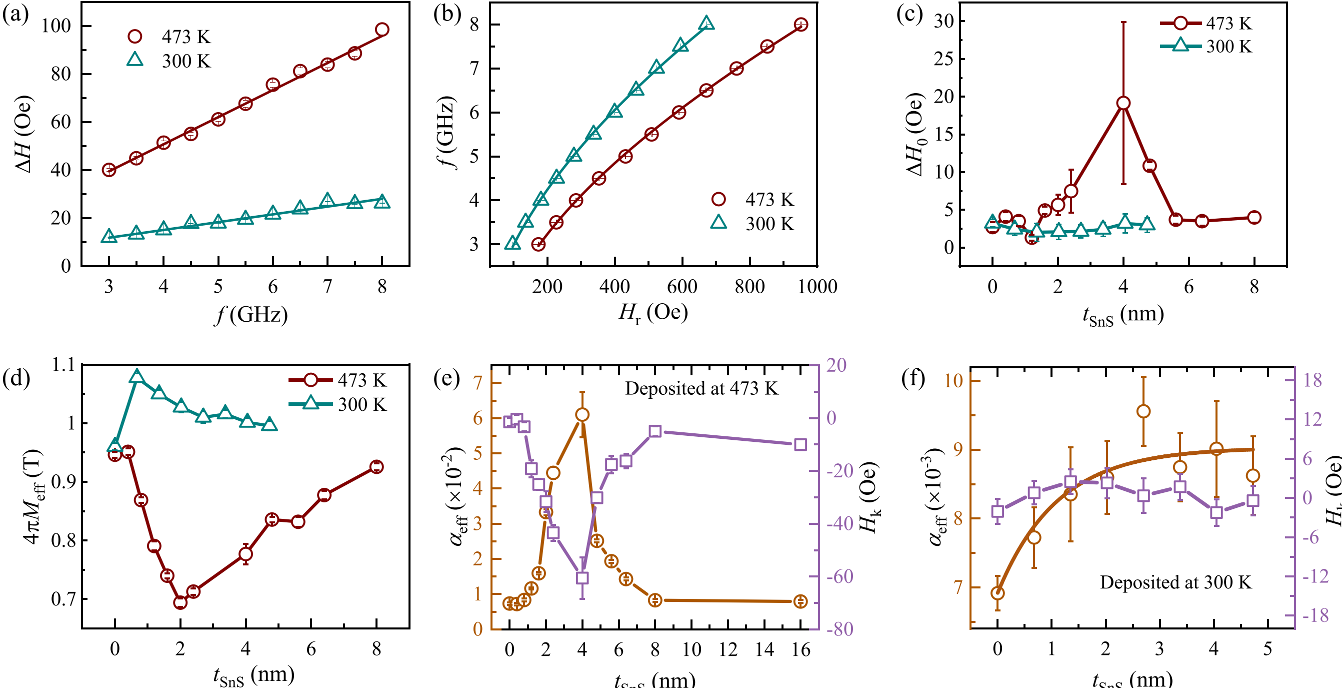

FIG. 4. (a) Linewidth (ΔH) as a function of RF frequency (f) for samples deposited at 473 K (open circle) and 300 K (open triangle). (b) f vs resonance field (H_r) plot with their corresponding best fit (solid line) using Eq. (2). Variation of (c) inhomogeneous line broadening (ΔH_0), and (d) effective saturation magnetization ($4\pi M_{eff}$) as a function of t_{SnS}. The trend of effective Gilbert damping parameter (α_{eff}) and uniaxial anisotropy field (H_k) as a function of t_{SnS} for sample deposited at (e) 473 K and (f) 300 K.

shape function to extract the resonance field and the linewidth. We fabricated microstrip devices that are 40 μm long and 10 μm wide for the STFMR measurements based on the lift-off technique using optical lithography. We applied an RF current and measured the DC voltage simultaneously using a bias tee [Fig. 5(a)]. R&S signal generator (SMB 100 A) was used to supply RF power of +3 dBm. The rectified DC voltage was detected using an amplitude modulation-based technique [34]. The magnetic field was applied at an angle φ with respect to the current direction. The angle φ was varied from (0–360 degrees) with the help of a vector field magnet (GMW 5201 projected field magnet).

III. RESULTS AND DISCUSSION

A. Growth of SnS films by PLD

Figure 1(b) shows the grazing incidence XRD spectra of the SnS thin films grown at various substrate temperatures (T_S = 300 to 523 K). In all the samples, we observe diffraction from just two planes that belong to the orthorhombic SnS structure [29], indicating no impurity phase. At 300 K, we observe only one diffraction peak corresponding to the (400) plane showing preferential [100] orientation. Above 473 K, the intensity of the (400) peak diminished appreciably, and the (011)-peak became prominent. We chose T_S = 300 K and 473 K to prepare SnS films with different thicknesses for the spin pumping study. The growth rate was determined by fitting the x-ray reflectivity (XRR) data using the recursive theory of Parratt [35], as shown in Fig. 1(c). From the XRR fitting, the growth rate of samples deposited at 300 K and 473 K was found to be 0.65 and 0.4 nm/sec, respectively.

We next performed the Raman spectroscopy measurements to characterize the vibrational properties of the SnS thin films. Figures 1(d) and 1(e) show the SnS thickness (t_{SnS}) dependent Raman data for SnS samples deposited at 473 K and 300 K, respectively. For both the growth temperature, four characteristic peaks of SnS [36] corresponding to A_g (at 95.4, 187.8, and 222.4 cm^{-1}) and B_{3g} (at 162.4 cm^{-1}) modes were observed for $t_{SnS} \geqslant 3$ nm (5 layers of SnS). Nonetheless, sharp Raman peaks could be observed for few-layered SnS thin films at a much lower thickness as compared to other works in literature [28,37], which highlights the superior quality of our PLD-grown SnS thin films. Further, we performed Raman measurements at ten different spots on a large-area ($\sim 1 \times 1$ cm^2) SnS thin film of thickness 5.4 nm prepared at 300 K, as shown in Fig. 1(f), which confirms a uniform large-area growth of 2D-SnS thin films.

XPS measurements were performed to assess the chemical states of Sn and S and to understand the surface chemistry of SnS thin films. Figure 2(a) represents the XPS survey scan showing core levels of Sn and S with no signature of impurity elements in our samples. The high-resolution Sn 3d XPS spectrum shows [Fig. 2(b)] two core level (CL) peaks corresponding to $3d_{5/2}$ and $3d_{3/2}$ at the binding energies (B.E.) of 486.0 and 494.3 eV, respectively, with peak separation of 8.3 eV which can be attributed to the Sn^{2+} chemical state [38,39]. In addition, the high-resolution S 2p spectrum [Fig. 2(c)] shows the doublet corresponding to $2p_{3/2}$ and $2p_{1/2}$ at the binding energies of 161.3 and 162.6 eV, respectively, suggesting the presence of S in the −2 reduced state [38]. The XPS results suggest that a pure SnS phase is formed on the Si/SiO_2 substrate. To establish the ferroelectric nature of

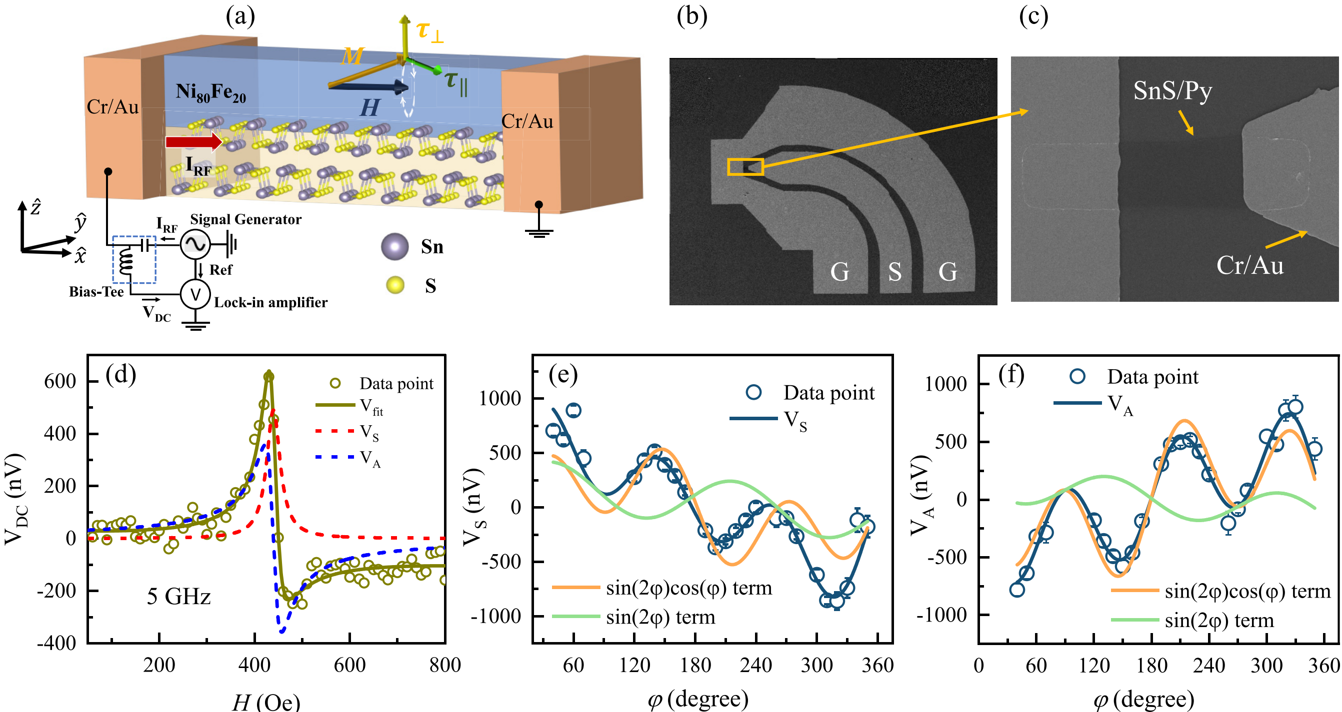

FIG. 5. (a) Schematic illustrating STFMR measurements setup and SnS/Py bilayer microstrip device with in-plane ($\tau_\parallel$) and out-of-plane ($\tau_\perp$) torque generated by the electric current along the x direction. (b), (c) Scanning electron microscopy (SEM) image of the STFMR device. (d) The STFMR spectra (open symbols) of SnS(1.3 nm)/Py(8 nm) sample at 5 GHz frequency, where red and blue dotted curves represent the symmetric (V_S) and antisymmetric (V_A) components of the rectified voltage, respectively. (e), (f) The angular dependence of V_S and V_A components, respectively.

the SnS, we prepared a step of SnS via the lift-off technique. Figures 2(d) and (e) represent the AFM and lateral PFM scans, respectively. SnS is known to possess in-plane ferroelectricity [19–21,39]. The in-plane component of the ferroelectric polarization can be detected by performing lateral PFM, which detects the lateral deflection of the cantilever due to bias-induced surface shearing [40]. For lateral PFM, the cantilever was first set at a contact resonance of around 1 MHz. Figure 2(e) presents the amplitude of the PFM response near the SnS step. Lateral PFM amplitude clearly shows a contrast between SnS and Si/SiO_2 substrates, confirming the ferroelectric nature of the SnS.

The RMS roughness of all the samples is summarized in Fig. 2(f) as a function of t_{SnS}. The AFM images are presented in Figs. S1 and S2 of the Supplemental Material [41]. Samples prepared at 300 K exhibit very low RMS roughness of the order of < 0.2 nm. In contrast, the roughness first increases with t_{SnS} up to $t_{SnS} = 4$ nm, and then it decreases at higher thicknesses for $T_S = 473$ K. This behavior can be attributed to the Volmer-Weber or island growth mode of films, in which the roughness increases with thickness due to island formation and, subsequently, continuous films are formed at higher thicknesses. The AFM results are further supported by comparative SEM images shown in Fig. S3 [41], where one can clearly see a smooth, homogeneous surface for $T_S = 300$ K film growth and island type growth for $T_S = 473$ K. We acquired the EDX spectrum (Fig. S4) to determine the composition of SnS thin film, which came out to be nearly $Sn_{1.03\pm0.03}S_{1.00\pm0.02}$. The EDX mapping of the SnS samples deposited at 300 K is shown in Figs. S5(a) and (b) [41] for Sn and S, respectively, showing a homogeneous distribution of Sn and S throughout the scanned area.

B. Study of spin pumping in SnS/Py

Subsequently, to determine the suitability of our SnS films for spintronics applications, we deposited the Py layer on top of SnS using magnetron sputtering. The presence of the SnS layer after Py deposition was confirmed using Raman measurements, as shown in Sec. S4 of the supplemental materials [41]. Consequently, we investigated the spin pumping phenomenon in SnS/Py bilayer thin films using a CPW-based FMR setup [Fig. 3(a)]. Since these spin pumping measurements are performed on thin films, it allows for quick optimization of our SnS films for spin-orbit investigation. Figure 3(b) shows a representative FMR signal for samples deposited at 473 K (brown) and 300 K (cyan). The FMR signal is fitted with a sum of symmetric and antisymmetric Lorentzian function [5,33] to determine the values of linewidth (ΔH) and resonance field (H_R). The frequency (f) dependence of ΔH and H_R are shown in Figs. 4(a) and 4(b), respectively. This behavior can be fitted with the following equation:

$$\Delta H = \frac{2\pi\alpha_{\rm eff} f}{\gamma} + \Delta H_0, \tag{1}$$

$$f = \frac{\gamma}{2\pi}[(H_R + H_k)(H_R + H_k + 4\pi M_{\rm eff})]^{1/2}, \tag{2}$$

where $\gamma = 1.85 \times 10^2$ GHz/T is the gyromagnetic ratio [42], ΔH_0 is the inhomogeneous line broadening, $4\pi M_{\rm eff}$ is

effective saturation magnetization, $\alpha_{\rm eff}$ is the effective Gilbert damping parameter, and $H_{\rm k}$ is the uniaxial anisotropy field.

The trend of ΔH_0 [Fig. 4(c)] with $t_{\rm SnS}$ reveals that the magnetic inhomogeneities [43] change with $t_{\rm SnS}$ for samples deposited at 473 K, whereas it is < 3 Oe for SnS films deposited at 300 K. This trend matches well with the roughness of SnS films presented in Fig. 2(f), indicating that magnetic inhomogeneities arise due to the surface roughness of SnS films. Nevertheless, the behavior of ΔH with f is linear for both cases, indicating that two-magnon scattering (TMS) and magnon-drag effect are negligible in our samples since both mechanisms lead to nonlinear behavior [44,45]. The variation of $4\pi M_{\rm eff}$ [Fig. 4(d)], $\alpha_{\rm eff}$, and $H_{\rm k}$ [Fig. 4(e)] indicate that the quality of Py is degraded due to the high roughness of SnS films grown at 473 K. Hence, the trend of $\alpha_{\rm eff}$ shown in Fig. 4(e) for SnS samples deposited at 473 K can be explained based on the degradation of Py quality. In contrast, $4\pi M_{\rm eff}$ [Fig. 4(d)] and $H_{\rm k}$ [Fig. 4(f)] remains nearly constant with thickness, showing very high-quality growth of Py on top of SnS thin film prepared at 300 K. $\alpha_{\rm eff}$ initially increases with the $t_{\rm SnS}$, and then it saturates after $t_{\rm SnS} = 2$ nm. The variation of $\alpha_{\rm eff}$ with $t_{\rm SnS}$ is in agreement with the theory of spin pumping, which predicts [46]

$$\alpha_{\rm eff} = \alpha_{\rm Py} + \frac{g\mu_{\rm B}}{4\pi M_{\rm s}}\frac{1}{t_{\rm Py}}(1 - e^{-2t_{\rm SnS}/\lambda_{\rm SnS}}), \tag{3}$$

where $\alpha_{\rm Py}$ is the Gilbert damping of reference sample [Py(8 nm)/AlO$_x$(3 nm)], and $t_{\rm Py}$ is the thickness of the Py layer. From the fitting presented in Fig. 4(f), the effective spin mixing conductance ($g_{\uparrow\downarrow}$) and spin diffusion length of SnS ($\lambda_{\rm SnS}$) are estimated to be $(8.83 \pm 1.15) \times 10^{18}$ m^{-2} and (2.2 ± 0.9) nm, respectively. The value of $g_{\uparrow\downarrow}$ is comparable to the traditionally used heavy metals like Ta [33,47,48] and W [49,50]. The spin diffusion length of SnS, $\lambda_{\rm SnS}$, is reported for the first time in this work.

C. STFMR measurements on SnS/Py

We perform STFMR measurements by applying RF current along the x direction and magnetic field applied at an angle φ with respect to the current direction and in the film plane (xy plane), as illustrated in Fig. 5(a). The SEM image of the fabricated STFMR device is shown in Figs. 5(b) and 5(c). Figure 5(d) shows a typical STFMR spectrum of SnS(1.3 nm)/Py(8 nm) bilayer measured at a radio frequency of 5 GHz. The STFMR signal ($V_{\rm DC}$) can be well fitted using a combination of symmetric and antisymmetric Lorentzian function [51,52]

$$V_{\rm DC} = V_{\rm S}\frac{\Delta H^2}{\Delta H^2 + (H - H_{\rm R})^2} + V_{\rm A}\frac{\Delta H(H - H_{\rm R})}{\Delta H^2 + (H - H_{\rm R})^2}. \tag{4}$$

Here, $V_{\rm S}$ and $V_{\rm A}$ are the magnitude of the symmetric and antisymmetric components of $V_{\rm DC}$, which are associated with in-plane ($\tau_{\parallel}$) and out-of-plane ($\tau_{\perp}$) torque, respectively. To examine the presence of unconventional SOT in the SnS/Py system, we performed angle-dependent (φ) STFMR measurements. In the case of high symmetry materials, if the RF current is along the x direction, the spin polarization is along the y direction and both $V_{\rm S}$ and $V_{\rm A}$ show $\sin(2\varphi)\cos(\varphi)$ dependence [6]. However, if an additional out-of-plane spin polarization is also present, then a $\sin(2\varphi)$ term can be added to the angular dependence of $V_{\rm S}$ and $V_{\rm A}$, as shown below [53,54]:

$$V_{\rm S} \propto \tau_{\rm DL}^{\parallel}\sin(2\varphi)\cos(\varphi) + \tau_{\rm FL}^{\parallel}\sin(2\varphi), \tag{5}$$

$$V_{\rm A} \propto \tau_{\rm FL}^{\perp}\sin(2\varphi)\cos(\varphi) + \tau_{\rm DL}^{\perp}\sin(2\varphi), \tag{6}$$

where $\tau_{\rm DL}^{\parallel}$ and $\tau_{\rm DL}^{\perp}$ represent the in-plane and out-of-plane dampinglike torque, respectively. $\tau_{\rm FL}^{\parallel}$ and $\tau_{\rm FL}^{\perp}$ represent in-plane and out-of-plane fieldlike torques, respectively. Figures 5(e) and 5(f) present the φ dependent $V_{\rm S}$ and $V_{\rm A}$ components (open circle) and their best fit (blue curve) using Eqs. (5) and (6), respectively. We note that some potential artifacts from spin pumping or the spin Seebeck effect may contribute an additional $\sin\varphi$ dependence in Eq. (5) [55,56]. In our case, the data is very well fitted without $\sin\varphi$ term, showing a negligible contribution from these artifacts. Recently, another artifact due to resonance heating was also reported in STFMR measurements involving van der Waals material $ZrTe_2$ [57]. However, these effects were found for samples thicker than 10 nm. In our case, the SnS thickness is much lower, and the resistivity of SnS (112 Ω cm) [58] is several orders higher than the resistivity of Py (84 μΩ cm), as shown in Sec. S3 of the Supplemental Material [41]. Hence, we believe the artifacts due to resonance heating are negligible in our case. Thus, from the angle-resolved STFMR, we found a conventional in-plane dampinglike torque, $\tau_{DL}^{\parallel} \propto \hat{m} \times (\hat{m} \times \hat{y})$; an unconventional out-of-plane dampinglike torque, $\tau_{DL}^{\perp} \propto \hat{m} \times (\hat{m} \times \hat{z})$; and an in-plane fieldlike torque $\tau_{FL}^{\parallel} \propto \hat{m} \times \hat{z}$. The values of torque ratios $\tau_{DL}^{\parallel}/\tau_{FL}^{\perp}$, $\tau_{DL}^{\perp}/\tau_{FL}^{\perp}$, and $\tau_{FL}^{\parallel}/\tau_{FL}^{\perp}$ comes out to be $-(0.99 \pm 0.07)$, (0.14 ± 0.02), and $-(0.34 \pm 0.04)$, respectively. Interestingly, the value of $\tau_{DL}^{\parallel}/\tau_{FL}^{\perp}$ is higher than the WTe_2/Py system [10].

Since the crystal structure of SnS lacks mirror symmetry, an unconventional out-of-plane dampinglike SOT is theoretically possible [8]. At first instant, our observation of unconventional SOT in the SnS/Py system appears consistent with the theoretical predictions. However, the resistivity of SnS is several orders higher than the resistivity of Py. Hence, most of the current flows through the Py layer. Thus, we believe the SOTs cannot originate from the nonmagnetic SnS layer. However, as the current flows through the interface between SnS and Py, it can generate SOT due to interfacial effects such as the Rashba-Edelstein effect [4]. D. MacNeill *et al.* [10] observed an out-of-plane dampinglike torque due to the low crystalline symmetry of WTe_2. However, we have polycrystalline SnS films, and hence, a similar mechanism cannot give rise to the unconventional torque observed in our experiments. An unconventional in-plane fieldlike torque is also reported in $NbSe_2$ [14], which was attributed to the symmetry breaking induced by strain during the fabrication process. In our case, the observation of unconventional in-plane fieldlike torque may arise from a similar mechanism. It may also be caused by the nonequilibrium spin-swapping effect [59]. A more comprehensive STFMR study is required to extract the exact mechanism of unconventional torques. Nevertheless, the results clearly show that SnS can be used to create in-plane and out-of-plane torques. This feature,

together with the gate tunable ferroelectricity property of SnS, is highly promising for efficient spin-orbitronic devices.

IV. CONCLUSIONS

In summary, we have demonstrated high-quality large-area growth of SnS on Si/SiO_2 substrates using the PLD technique. We show that SnS films deposited at 300 K exhibit low surface roughness. We performed a detailed SnS thickness-dependent spin pumping measurement in the SnS/Py system for SnS films deposited at 300 K and 473 K. We show that the trend of Gilbert damping constant with the thickness of Py agrees with the theory of spin pumping only for SnS films grown at 300 K, which exhibit lower surface roughness. For these optimized SnS films at 300 K, we found a spin mixing conductance of (8.83 ± 1.15) nm^{-2} in the SnS/Py system. We also perform angular-dependent STFMR measurement, which reveals the presence of an unconventional SOT in the SnS/Py system. Though unconventional SOT is expected in SnS from the symmetry argument, our results show that the unconventional SOT in our system originates at the interface. Our demonstration of large area growth of SnS, the observation of out-of-plane dampinglike torque together with ferroelectric properties shows that SnS is a potential candidate for efficient spin-orbit-torque devices.

ACKNOWLEDGMENTS

The partial support from the Ministry of Human Resource Development under the IMPRINT program (Grants No. 7519 and No. 7058); the Department of Electronics and Information Technology (DeitY), Science & Engineering research board (SERB File no. CRG/2018/001012), Joint Advanced Technology Centre at IIT Delhi, Grand Challenge Project, IIT Delhi; and the Department of Science and Technology under the Nanomission program [Grant No. $SR/NM/NT-1041/2016(G)$] are gratefully acknowledged. We also acknowledge the nanoscale research facility, IIT Delhi, for fabrication facilities and the Department of Physics, IIT Delhi, for the pulsed laser deposition system. H.B. gratefully acknowledges the financial support from the Council of Scientific and Industrial Research (CSIR) Grant No. 09/086(1342) 2018-EMR-1, Government of India.

---

[1] A. D. Kent and D. C. Worledge, Nat. Nanotechnol. **10**, 187 (2015).
[2] J. Sinova, S. O. Valenzuela, J. Wunderlich, C. H. Back, and T. Jungwirth, Rev. Mod. Phys. **87**, 1213 (2015).
[3] H. Bangar, K. I. A. Khan, A. Kumar, N. Chowdhury, P. K. Muduli, and P. K. Muduli, Adv. Quantum Technol. **6**, 2200115 (2023).
[4] Q. Shao, G. Yu, Y. W. Lan, Y. Shi, M. Y. Li, C. Zheng, X. Zhu, L. J. Li, P. K. Amiri, and K. L. Wang, Nano Lett. **16**, 7514 (2016).
[5] H. Bangar, A. Kumar, N. Chowdhury, R. Mudgal, P. Gupta, R. S. Yadav, S. Das, and P. K. Muduli, ACS Appl. Mater. Interfaces **14**, 41598 (2022).
[6] A. Manchon, J. Železný, I. M. Miron, T. Jungwirth, J. Sinova, A. Thiaville, K. Garello, and P. Gambardella, Rev. Mod. Phys. **91**, 035004 (2019).
[7] K. L. Wang, X. Kou, P. Upadhyaya, Y. Fan, Q. Shao, G. Yu, and P. K. Amiri, Proc. IEEE **104**, 1974 (2016).
[8] Y. Liu and Q. Shao, ACS Nano **14**, 9389 (2020).
[9] H. Kurebayashi, J. H. Garcia, S. Khan, J. Sinova, and S. Roche, Nat. Rev. Phys. **4**, 150 (2022).
[10] D. MacNeill, G. Stiehl, M. Guimaraes, R. Buhrman, J. Park, and D. Ralph, Nat. Phys. **13**, 300 (2017).
[11] G. Yu, P. Upadhyaya, Y. Fan, J. G. Alzate, W. Jiang, K. L. Wong, S. Takei, S. A. Bender, L. T. Chang, Y. Jiang *et al.*, Nat. Nanotechnol. **9**, 548 (2014).
[12] W. Zhang, J. Sklenar, B. Hsu, W. Jiang, M. B. Jungfleisch, J. Xiao, F. Y. Fradin, Y. Liu, J. E. Pearson, J. B. Ketterson *et al.*, APL Mater. **4**, 032302 (2016).
[13] D. MacNeill, G. M. Stiehl, M. H. D. Guimaraes, N. D. Reynolds, R. A. Buhrman, and D. C. Ralph, Phys. Rev. B **96**, 054450 (2017).
[14] M. H. Guimaraes, G. M. Stiehl, D. MacNeill, N. D. Reynolds, and D. C. Ralph, Nano Lett. **18**, 1311 (2018).
[15] G. M. Stiehl, R. Li, V. Gupta, I. E. Baggari, S. Jiang, H. Xie, L. F. Kourkoutis, K. F. Mak, J. Shan, R. A. Buhrman, and D. C. Ralph, Phys. Rev. B **100**, 184402 (2019).
[16] M. Zhou, X. Chen, M. Li, and A. Du, J. Mater. Chem. C **5**, 1247 (2017).
[17] L. D. Zhao, G. Tan, S. Hao, J. He, Y. Pei, H. Chi, H. Wang, S. Gong, H. Xu, V. P. Dravid *et al.*, Science **351**, 141 (2016).
[18] R. Fei, W. Li, J. Li, and L. Yang, Appl. Phys. Lett. **107**, 173104 (2015).
[19] M. Wu and X. C. Zeng, Nano Lett. **16**, 3236 (2016).
[20] R. Fei, W. Kang, and L. Yang, Phys. Rev. Lett. **117**, 097601 (2016).
[21] Y. Bao, P. Song, Y. Liu, Z. Chen, M. Zhu, I. Abdelwahab, J. Su, W. Fu, X. Chi, W. Yu *et al.*, Nano Lett. **19**, 5109 (2019).
[22] N. Higashitarumizu, H. Kawamoto, C. J. Lee, B. H. Lin, F. H. Chu, I. Yonemori, T. Nishimura, K. Wakabayashi, W. H. Chang, and K. Nagashio, Nat. Commun. **11**, 2428 (2020).
[23] C. Dagdeviren, Y. Su, P. Joe, R. Yona, Y. Liu, Y. S. Kim, Y. Huang, A. R. Damadoran, J. Xia, L. W. Martin *et al.*, Nat. Commun. **5**, 4496 (2014).
[24] V. Garcia, S. Fusil, K. Bouzehouane, S. Enouz Vedrenne, N. D. Mathur, A. Barthelemy, and M. Bibes, Nature (London) **460**, 81 (2009).
[25] Z. Tian, C. Guo, M. Zhao, R. Li, and J. Xue, ACS Nano **11**, 2219 (2017).
[26] L. Liu, C. Zhou, X. Shu, C. Li, T. Zhao, W. Lin, J. Deng, Q. Xie, S. Chen, J. Zhou *et al.*, Nat. Nanotechnol. **16**, 277 (2021).
[27] J. Su, X. Wang, C. Shao, Y. Guo, and L. Xian, Mater. Des. **209**, 110005 (2021).
[28] W. Wang, T. Zhang, A. Seliverstov, H. Zhang, Y. Wang, F. Wang, X. Peng, Q. Lu, C. Qin, X. Pan *et al.*, Adv. Electron. Mater. **6**, 1901020 (2020).
[29] F. Y. Ran, Z. Xiao, H. Hiramatsu, K. Ide, H. Hosono, and T. Kamiya, AIP Adv. **6**, 015112 (2016).

[30] J. R. Brent, D. J. Lewis, T. Lorenz, E. A. Lewis, N. Savjani, S. J. Haigh, G. Seifert, B. Derby, and P. O'Brien, J. Am. Chem. Soc. **137**, 12689 (2015).
[31] H. Kawamoto, N. Higashitarumizu, N. Nagamura, M. Nakamura, K. Shimamura, N. Ohashi, and K. Nagashio, Nanoscale **12**, 23274 (2020).
[32] F. Y. Ran, Z. Xiao, H. Hiramatsu, H. Hosono, and T. Kamiya, Appl. Phys. Lett. **104**, 072106 (2014).
[33] A. Kumar, R. Bansal, S. Chaudhary, and P. K. Muduli, Phys. Rev. B **98**, 104403 (2018).
[34] A. Kumar, R. Sharma, K. I. Ali Khan, C. Murapaka, G. J. Lim, W. S. Lew, S. Chaudhary, and P. K. Muduli, ACS Appl. Electron. Mater. **3**, 3139 (2021).
[35] L. G. Parratt, Phys. Rev. **95**, 359 (1954).
[36] H. Chandrasekhar, R. Humphreys, U. Zwick, and M. Cardona, Phys. Rev. B **15**, 2177 (1977).
[37] J. Xia, X. Z. Li, X. Huang, N. Mao, D. D. Zhu, L. Wang, H. Xu, and X. M. Meng, Nanoscale **8**, 2063 (2016).
[38] H. Choi, J. Lee, S. Shin, J. Lee, S. Lee, H. Park, S. Kwon, N. Lee, M. Bang, S. B. Lee *et al.*, Nanotechnology **29**, 215201 (2018).
[39] H. Khan, N. Mahmood, A. Zavabeti, A. Elbourne, M. Rahman, B. Y. Zhang, V. Krishnamurthi, P. Atkin, M. B. Ghasemian, J. Yang *et al.*, Nat. Commun. **11**, 3449 (2020).
[40] L. Eng, H. J. Güntherodt, G. Rosenman, A. Skliar, M. Oron, M. Katz, and D. Eger, J. Appl. Phys. **83**, 5973 (1998).
[41] See Supplemental Material at http://link.aps.org/supplemental/10.1103/PhysRevMaterials.7.094406 for surface morphology and roughness analysis; composition analysis; restivity of SnS and Py samples; and the Raman data before and after Py deposition. It also contains Ref. [58].
[42] J. M. Shaw, H. T. Nembach, T. J. Silva, and C. T. Boone, J. Appl. Phys. **114**, 243906 (2013).
[43] M. Farle, Rep. Prog. Phys. **61**, 755 (1998).
[44] R. Arias and D. L. Mills, Phys. Rev. B **60**, 7395 (1999).
[45] Y. Li, Y. Li, R. Sun, J.-N. Liu, N. Li, X. Yang, Z.-Z. Gong, Z.-K. Xie, W. He, X.-Q. Zhang *et al.*, J. Phys.: Condens. Matter **33**, 175801 (2021).
[46] J. Foros, G. Woltersdorf, B. Heinrich, and A. Brataas, J. Appl. Phys. **97**, 10A714 (2005).
[47] R. Yu, B. F. Miao, L. Sun, Q. Liu, J. Du, P. Omelchenko, B. Heinrich, M. Wu, and H. F. Ding, Phys. Rev. Mater. **2**, 074406 (2018).
[48] E. Montoya, P. Omelchenko, C. Coutts, N. R. Lee Hone, R. Hübner, D. Broun, B. Heinrich, and E. Girt, Phys. Rev. B **94**, 054416 (2016).
[49] P. Deorani, J. Son, K. Banerjee, N. Koirala, M. Brahlek, S. Oh, and H. Yang, Phys. Rev. B **90**, 094403 (2014).
[50] Q. Lu, Y. Li, B. Peng, H. Tang, Y. Zhang, Z. He, L. Wang, C. Li, W. Su, Q. Yang *et al.*, Phys. Rev. Appl. **12**, 064035 (2019).
[51] L. Liu, T. Moriyama, D. C. Ralph, and R. A. Buhrman, Phys. Rev. Lett. **106**, 036601 (2011).
[52] Y. You, H. Bai, X. Feng, X. Fan, L. Han, X. Zhou, Y. Zhou, R. Zhang, T. Chen, F. Pan, and C. Song, Nat. Commun. **12**, 6524 (2021).
[53] J. Zhou, X. Shu, Y. Liu, X. Wang, W. Lin, S. Chen, L. Liu, Q. Xie, T. Hong, P. Yang *et al.*, Phys. Rev. B **101**, 184403 (2020).
[54] T. Nan, C. X. Quintela, J. Irwin, G. Gurung, D.-F. Shao, J. Gibbons, N. Campbell, K. Song, S. Y. Choi, L. Guo *et al.*, Nat. Commun. **11**, 4671 (2020).
[55] W. L. Yang, J. W. Wei, C. H. Wan, Y. W. Xing, Z. R. Yan, X. Wang, C. Fang, C. Y. Guo, G. Q. Yu, and X. Han, Phys. Rev. B **101**, 064412 (2020).
[56] Q. Fu, L. Liang, W. Wang, L. Yang, K. Zhou, Z. Li, C. Yan, L. Li, H. Li, and R. Liu, Phys. Rev. B **105**, 224417 (2022).
[57] T. M. Cham, S. Karimeddiny, V. Gupta, J. A. Mittelstaedt, and D. C. Ralph, Adv. Quantum Technol. **5**, 2100111 (2022).
[58] T. Garmim, S. Chahib, L. Soussi, R. Mghaiouini, Z. E. Jouad, A. Louardi, O. Karzazi, M. E. Jouad, E. Hlil, B. Hartiti *et al.*, J. Mater. Sci. Mater. Electron. **31**, 20730 (2020).
[59] C. O. Pauyac, M. Chshiev, A. Manchon, and S. A. Nikolaev, Phys. Rev. Lett. **120**, 176802 (2018).